Computational Study of Shock Mitigation and Drag Reduction by Pulsed Energy Lines

Kevin Kremeyer*
PM & AM Research, Tucson, Arizona 85719
Kurt Sebastian[†]
U.S. Coast Guard Academy, New London, Connecticut 06320
and
Chi-Wang Shu[‡]
Brown University, Providence, Rhode Island 02912

A series of numerical experiments were performed in which energy was deposited ahead of a cone traveling at supersonic/hypersonic speeds. The angle of attack was zero, and the cone half-angles ranged from 15 to 45 deg. The Mach numbers simulated were 2, 4, 6, and 8. The energy was deposited instantaneously along a finite length of the cone axis, ahead of the cone's bow shock, causing a cylindrical shock wave to push air outward from the line of deposition. The shock wave would sweep the air out from in front of the cone, leaving behind a low-density column/tube of air, through which the cone (vehicle) propagated with significantly reduced drag. The greatest drag reduction observed was 96%. (One-hundred percent drag reduction would result in the complete elimination of drag forces on the cone.) The propulsive gain was consistently positive, meaning that the energy saved as a result of drag reduction was consistently greater than the amount of energy "invested" (i.e., deposited ahead of the vehicle). The highest ratio of energy saved/energy invested was approximately 6500% (a 65-fold "return" on the invested energy). We explored this phenomenon with a high-order-accurate multidomain weighted essentially nonoscillatory finite difference algorithm, using interpolation at subdomain boundaries. This drag-reduction/shock-mitigation technique can be applied locally or globally to reduce the overall drag on a vehicle.

Nomenclature

a_0	=	speed of sound
b	=	3.94 (constant within Plooster characteristic radius)
D_{cb}	=	drag-along cone base
D_{cs}	=	drag-along cone sides
D_{tot}	=	total drag-along cone
E_0	=	Plooster study energy deposited per unit length
M	=	Mach number
p	=	pressure
R_0	=	Plooster study characteristic radius
r	=	Plooster study dimensional radius
u_r	=	radial-velocity component
u_x	=	axial-velocity component
u_θ	=	azimuthal-velocity component
γ	=	1.4 (ratio of specific heats for air)
λ	=	Plooster study dimensionless radius
ρ	=	density

I. Introduction

THE objective of this paper is to describe and characterize a flow-control/drag-reduction method for supersonic/hypersonic flight. We have numerically performed many experiments using a multidomain weighted essentially nonoscillatory (WENO) finite difference method developed in Ref. 1 to compute the three-dimensional axisymmetric Euler equations. The robustness and validation of this method for recognized test cases is demonstrated extensively in Ref. 1; however, this current example is the first time calculations of this geometric complexity were computed using a high-order finite difference method. To our knowledge, simulation for this specific problem has not been performed before. Therefore, there are no known reliable sources against which to compare the numerical results, other than some coarse steady-state pressure measurements at the cone, which appear later in Table 1. Figure 1 displays one of our numerical results. It is qualitatively clear from this figure that the drag on the conical vehicle can be significantly reduced by the opening up of a low-density core ahead of the vehicle on its flight axis. This, in conjunction with cursory qualitative wind-tunnel experiments, motivated further study, and in the paper we describe the quantitative results of our many experiments, which led to as much as 96% drag reduction.

II. Energy Deposition in Supersonic Flows

A. Motivation for the Experiments

Hypersonic and supersonic vehicles generate shock waves, which are accompanied by a host of technical challenges. These include increased drag, sonic boom, and destructively high temperatures and pressures on both airframe and components. "Suddenly" (as opposed to "gently") heating an extended path of air, ahead of the shock wave and along the vehicle's velocity vector, results in rapid expansion of the heated air. This creates a long, hot, low-density core, into which the vehicle's bow shock expands, followed by the vehicle itself (see again Fig. 1). Strategically heating extended regions of gas ahead of the vehicle can therefore mitigate the shock wave, as well as its deleterious effects. Also, because the vehicle will preferentially fly along the low-density channel (i.e., be partially steered by it), adjusting the direction of hot core formation can be utilized as a method of control. The benefits of this technology therefore include tremendous increases in fuel efficiency and control, which remain outstanding problems in all supersonic/hypersonic platforms.

*Vice President of Research; kremeyer@physics-math.com. Associate Fellow AIAA.
[†]Associate Professor, Department of Mathematics; also Visiting Research Scholar, Division of Applied Mathematics, Brown University, Providence, RI 02912; ksebastian@exmail.uscga.edu. Member AIAA.
[‡]Professor, Division of Applied Mathematics; shu@dam.brown.edu.

Table 1 Verification table for computed steady-state drag[a]

| Mach	Analytical SSD[b,c,d]	Computed SSD[b,e]	% Difference
2	3.818	3.842	0.63
4	10.889	10.871	0.17
6	22.203	22.270	0.30
8	37.761	38.534	2.05

[a]All computations are for a cone with a 30-deg half-nose angle at zero angle of attack.
[b]SSD is the steady-state drag value.
[c]The analytical SSD was determined from the work by Sims,[53] corrected using the experimentally verified $-1/M^2$ approximation of the base pressure coefficient found in Ref. 52.
[d]It is clear that we have obtained good agreement with the analytical SSD with no more than a 2.05% error.
[e]The computed SSD was determined from our numerical simulations of the axisymmetric Euler equations with our multidomain WENO method.
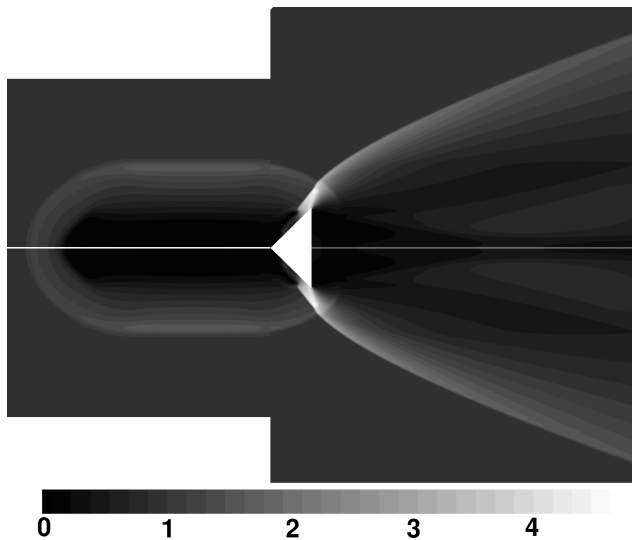
Fig. 1 Three-dimensional axisymmetric numerical simulation of a conical vehicle in supersonic flight showing density contours for a pulsed energy line deposited before the cone. An extended path is heated ahead of the cone in supersonic flow, creating a low-density core through which the vehicle can travel, thereby significantly reducing the drag on the cone.

In addition to drag reduction and flow control, effective shock-wave mitigation will also decrease ablation/heat-resistance requirements of critical surfaces and components. The potential result is therefore faster, more durable/maneuverable systems, with increased kinematic footprints. Our calculations and simulations predict a reduction in wave drag of more than 90%, with a return ratio [defined as the ratio of the thrust (power) saved over the invested power] of ~10:1 for a streamlined body and ~65:1 for a bluff body. The electromagnetic nature of this technology addresses the desire to move away from complex actuator systems and control surfaces, whereas the technology's nonmechanical ability to "streamline" arbitrary bodies addresses the desire to reduce both time and cost of design, development, and maintenance. It allows manufacturers to approach the ideal situation of designing an airframe around its payload and mission, while depending on an electro-optic system to take care of the streamlining for them. A very long, low-density path, opened up ahead of an airframe, will provide any vehicle with a much more favorable "effective aspect ratio," allowing it to propagate through the low-density tube, with greatly reduced resistance.

The potential benefits of this technology span the applications of high-speed flight. Reducing drag reduces fuel requirements and therefore translates directly into lower weight and/or greater range/payload. Furthermore, the associated reduction in heating/pressure translates into less stringent materials requirements, less damage, and/or increased performance envelopes. A third major benefit is the decreased environmental (acoustic) impact of high-speed vehicles, in the form of sonic-boom mitigation. The

combination of all of these benefits stands to increase kinematic footprint through greater speed and range with a lower acoustic signature.

In the past, air has been "pushed" laterally out of the way of a moving vehicle by using an aerospike. The approach described here offers the possibility of pushing air laterally out of a vehicle's way, tens, even hundreds of meters ahead of the vehicle. This method is all the more alluring because the pushing is performed without the impediment of a physical spike, which can actually become a liability when the vehicle is moving at a nonoptimized angle of attack.

Another benefit is apparent in applying this technology to develop a new maneuvering (control) method, which is more efficient at higher Mach numbers. This approach represents an excellent opportunity for us to overcome the problems of the supersonic implementation of traditional control methods, which have oftentimes evolved from subsonic applications. An example of localized flow control using energy deposition is the mitigation of detrimental effects of a shock/shock interaction on an air vehicle during maneuver. Shock/shock interactions can occur on supersonic and hypersonic aircraft during maneuver and sustained flight. For example, oblique shock waves propagating from the nose of an aircraft or missile can interact with the bow shock of any body protruding from the fuselage, for example, stabilizing fins, external payloads, booster rockets, engine cowls, and inlets. Some shock/shock interactions can lead to severe and often catastrophic events for aircraft.

B. Past Work

Shock waves have traditionally been studied and characterized during propagation through a medium, free of fluctuations over length scales characteristic of the driving body. More recently, however, the investigation of such disturbances has become increasingly common. In fact, the last decade has seen an increased interest in controlling/mitigating shock waves by modifying/controlling the gas ahead of them. Historically, one of the first attempts to do this was with a long, thin spike at the tip of the vehicle. Such an aerospike generally protrudes well ahead of the vehicle nose, creating its own shock wave, and significantly reduces the drag on the vehicle. This technique is still being investigated, for example, by Guy et al.[2] and by Nemchinov et al.,[3] who took it even further by looking at shock interaction with a heated "hot" spike. Other mechanical methods of affecting the shock wave have also been researched over the decades, including counterpropagating streams of gas,[4,5] heated/reacting/ionized gas,[6] and liquid (e.g., water) and even using an ablative aerospike (e.g., Teflon[TM]) to deposit its degradation products into the flow.

The benefits of these methods have typically been reported when applied to bluff bodies, and all have reported drag reduction as high as 50%. One complaint of such reported benefits is that they often merely approach the savings that can be achieved by using a more aerodynamic body. Another problem is that all of the "counterflow" methods are similar to the solid/rigid aerospike, in that they also physically push forward against the air. As a result, these methods also suffer from the fundamental mechanical limitation of forming their own shock wave, that is, they are unable to "get ahead" of a shock.

An intuitive means to circumvent this limitation is to use electromagnetic radiation to affect the air ahead of a shock. This has also been investigated over the past several decades. One of the initial electromagnetic methods investigated was to ionize the gas ahead of the shockwave. This was accomplished in a number of different ways, including rf and dc plasmas.[7-9] For years, the observed effects had commonly been attributed to an interaction of electrons/ions with the shock wave. However, a number of groups working simultaneously[10-18] led toward the gradual acceptance that the primary factor in the observed dynamics is thermal. Experimental efforts by Merriman et al.[19] and Ionikh et al.[20] then began to concur with the work of these groups. A thorough documentation of the Russian literature is included by Macheret et al. in Ref. 14, and Fomin et al. in Ref. 21 have included a review of different methods of plasma control. Despite the more balanced understanding of

thermal effects within different communities, there do remain finer effects of ionization, which continue to be investigated.[22−24]

In the course of numerically investigating shock propagation through various density and temperature profiles, Kremeyer et al.[25] noted the increased shock speed and decreased pressure jump experienced when a shock wave encountered a heated swath of gas. The most dramatic effect, by far, was obtained when the swath (strip) was aligned with the direction of shock propagation (resulting in the shock making a "T" with the heated swath of gas). The effect was present even for a very narrow strip, and it was strongest when the temperature in the strip was highest. Because of the higher speed of sound within the hot swath, the most apparent feature was for the shock to bulge forward as it propagated into the heated region. The pressure jump across the bulged region of the shock was also lowered. In general, when propagating into a time-invariant and relatively moderate temperature cross section, the shock structure adopts a steady shape and constant speed. Behind the shock, a flow pattern establishes itself to allow the steady shape to persist and to continue propagating. In contrast, a much more dramatic effect is observed when the swath is sufficiently heated (yielding a high enough speed of sound) to effectively eliminate the local pressure jump. (In a practical sense, this occurs when the speed of sound in the heated swath is greater than the vehicle speed.) In this case, the shock is effectively "punctured," allowing the high-pressure fluid (formerly fully contained behind the shock) to flow freely forward along the hot path. This creates a forward-propagating, low-density jet, along which the more highly compressed neighboring fluid (behind the "unpunctured" shock) can be entrained and escape forward as well. Creating such a strongly heated swath ahead of the bow shock of a supersonic vehicle therefore allows a release of the high-pressure gas behind the shock wave. This effect can be exploited to strategically reduce the local drag/pressure on the vehicle to aid in maneuvering. For the greatest overall drag reduction, a path can be heated along the vehicle's stagnation line.

Providing a mechanism to help realize the desired energy-deposition geometries, ultrashort laser technologies can use laser radiation to produce extended swaths of hot, ionized gas. Typically, when an energetic laser is focused to a point to ionize air, the resulting plasma disperses the beam/pulse. In a large parameter range, however, high-energy pico- and femtosecond laser pulses have actually been found to propagate over large distances, while heating and ionizing gas in their path. This phenomenon is referred to as filamentation.[26] It has also been observed using wavelengths ranging from the infrared to UV,[27] pulse durations from picoseconds to tens of femtoseconds, and pulse energies from millijoules to joules. Spatially, the filamenting pulses have been reported to extend over hundreds of meters, and the filament diameters have been reported to range from 0.1 to several millimeters.[28,29] The laser pulse can be focused and adjusted to control the point at which filamentation begins and ends, and the rapid expansion caused by the gas heating can result in an audible "crack" or "snap." Current work indicates that ionized filaments, which propagate over kilometers, can be obtained with nanosecond UV lasers, given sufficient pulse power/energy.[30]

In response to the preceding observations and developments, a number of implementations have been developed to take advantage of this novel geometry.[31] Some of these implementations involve the use of laser pulses to heat the gas ahead of the shock wave. The use of lasers to heat the air ahead of a shock wave is not new.[32−34] "Filaments" have also been discussed in the literature in the form of filamenting arcs in microwave/hf discharges by Leonov et al.[10] and by Cain and Boyd.[11] The geometry we model in this paper is distinct, however, in that the methods investigated in the past were not capable of creating a long, narrow, and straight path of heated gas, which can be scaled up to large dimensions (e.g., heated paths hundreds of meters long). Past laser-heating methods have primarily depended on focusing their energy to a point ahead of the shock wave. These can generate slightly extended regions of hot/ionized gas, but not the long paths required for optimal pressure release. To achieve long, ionized paths, one can use a number of methods, including weakly focused UV pulses and filamenting lasers. To further increase the energy deposition, bundles of filaments can be used, or

an electric discharge can be guided along the laser-ionized path.[35] This technique provides a very efficient method of quickly heating a line of air. The rapidly deposited energy of such heating methods not only creates a low-density swath of gas, but also results in the necessary cylindrical shock wave propagating outward from the originally heated path (described in the next section).

As the vehicle moves forward into the heated swath, the cylindrical shock wave continues to propagate outward. Therefore, the vehicle sees a gradually widening low-density region with its enveloping cylindrical shock wave expanding outward. (The cylindrical shock wave eventually degrades to a sound wave as a result of the expansion.) The air left inside of the expanding cylindrical shock wave remains elevated to a higher temperature, with a lower density and higher speed of sound than the original ambient air. This residual or "ancillary" heating has been meticulously characterized by Plooster[36] and yields the drag-reduction benefits investigated in this paper. The net heating on an air frame when propagating through this higher-temperature, lower-density core is greatly decreased from the temperatures that would result from propagating through full-density, lower-temperature air.

C. Creating a Low-Density Core

Over the decades, the evolution of large amounts of energy concentrated along point and line sources has been thoroughly characterized.[36−39] In his meticulous computational study, Plooster[36] provides his data in dimensionless units for an infinite line source of energy. In all of his graphs, the energy is deposited at $r = 0$, and the distance from this origin (in one-dimensional cylindrical coordinates) is described using the dimensionless radius λ. In each graph, λ is plotted along the abscissa, and it represents the ratio of the true distance r to a characteristic radius $R_0 = (E_0/b\gamma p_0)^{1/2}$, where p_0 is the pressure ahead of the shock. Plooster realized shortly after publishing his work in Ref. 36 that he made a small error in calculating this characteristic radius. In Ref. 40, he published an erratum that states instead $R_0 = (4E_0/b\gamma p_0)^{1/2}$. This true characteristic radius is used henceforth in this paper. Several plots are drawn on each graph, with numbers above each individual line. These numbers represent the dimensionless time τ, which is the ratio of the real time t to a characteristic time $t_0 = R_0/a_0$, where a_0 is the speed of sound in the ambient atmosphere ahead of the shock wave.

Additional utility of these results comes from the fact that Plooster verified them for a variety of initial conditions. The long-term dynamics (of interest to us) are basically identical for initial conditions ranging from ideal line sources to more diffuse sources. The results are presumably robust enough to further encompass any method that we can conceive to deposit energy along an extended region ahead of the shock wave we would like to mitigate/control.

As the shock wave propagates radially outward, a rarefaction begins to develop behind the expanding shock wave at approximately $\tau = 0.2$. This ultimately results in a reversed flow at approximately $\tau = 0.56$ when the gas near this rarefaction begins to flow back toward the origin, instead of continuing to flow outward.

It is at this point of flow reversal that the most important feature of these dynamics becomes "locked in." From approximately $\tau = 0.56$ to well beyond $\tau = 6.0$, a very low-density core, within the expanding cylinder of air, remains effectively stationary and unchanged from $\lambda = 0$ to approximately $\lambda = 0.5$. The beauty and utility of this arbitrarily long, low-density cylindrical core is that it persists for a very long time and can be used as a low-density channel, through which a vehicle (and/or the high-pressure air being pushed by it) can travel. Thermal diffusion is far too slow to significantly alter the core before the vehicle passes through it.

The parameters and scales from Plooster's results were used to estimate the energy/power requirements for our test cases. The simulations are intended to show the compelling advantage in shock mitigation and drag reduction when suddenly depositing heat along a streamline ahead of a shock wave. The sustained benefit, demonstrated in the line-deposition geometry, results in extended periods of shock mitigation/drag reduction, without continual energy addition. This allows the heating mechanism to be operated in a pulsed mode. Once the energy is deposited, a long path of air is heated. This

path expands according to the dynamics reported by Plooster.[36] His results show that the internal low-density core (which we would like to exploit) is fully developed by approximately $\tau = 0.34$ and is usable until at least $\tau = 6.0$.

D. General Energy Estimates

Given the preceding considerations of Plooster, we can make rough estimates of the energy required per pulse for effective shock control/drag reduction. Such rough considerations take into account only the low-density core ahead of the vehicle. Two neglected nonlinear effects are the fluid's lateral velocity and the recirculation pressure behind the vehicle. As a result of the high-density air channeled around the vehicle, the pressure behind it actually has the potential to be raised, resulting in not only a low-density channel for the vehicle to propagate into, but also a higher pressure behind the vehicle to help push it forward. A more encompassing analysis requires much more careful simulations and experiments to investigate these full effects. Our first step in this direction has been to perform the simulations using a multidomain high-order-accurate WENO finite difference computational-fluid-dynamics code developed in Ref. 1. An in-depth explanation of this effort can be found in Sec. III of this paper on numerical results.

The standard feature that we will use to discuss the aerodynamic benefit is the low-density core, which Plooster showed to extend to approximately $\lambda = 0.5$ (Fig. 4 in Ref. 36). If we would like the radius of this core to be $\frac{1}{2}$ of the vehicle radius, we can calculate the necessary energy deposition per length E_0 using the definition of $\lambda = r/R_0$, where $R_0 = (4E_0/5.34 \times p_0)^{\frac{1}{2}}$ and p_0 is the ambient air pressure. This gives us the energy per length necessary to create a low-density core of radius r. First we rearrange to get $E_0 = 5.34 \times p_0 \times R_0^2/4$. Then, expressing R_0 in terms of λ and r, we obtain $E_0 = 1.33 \times p_0 \times (r/\lambda)^2$. The main value of λ, about which we care, is $\lambda = 0.5$ because this is the approximate dimensionless width of the low-density core. A primary dimension, which provides us with physical information, is the actual radius r of the low-density core we would like to create. As can be expected, the energy per length required to create a given low-density core is proportional to the square of its radius (i.e., proportional to its cross-sectional area) $E_0 = 5.34 \times p_0 \times r^2$. To obtain the total energy required, we must simply multiply E_0 by the length of the heated path. This length is one of the system parameters that must be investigated in the testing phase, and it also plays a role in determining the pulse repetition rate (which will also be investigated during testing). However, one can choose nominal values to estimate ranges of pulse energy and average power.

One approach of heating the gas ahead of a vehicle is to prevent "breaks" in the hot path by creating each new low-density core so that its front end is butted up against the preceding core's back. However, one possible way to save on power and total energy deposition is to leave a break of unheated air between the successive individual cores. This will allow us to exploit some of the time required for the shockwave to actually reform ahead of the vehicle. As the vehicle's shock wave is reforming, the next heated core will break it up again. In practice, the optimal ratio of the hot-core length to the unheated length will have to be determined with wind-tunnel tests and additional detailed simulations.

E. Heating/Shock-Wave Interaction: Past Work

The reason for discussing the preceding method(s) to heat an extended path of air is its direct applicability to the control/mitigation of a shock wave. We recall here time-resolved studies of point heating in front of a shock wave.

The beautiful time-resolved wind-tunnel studies of Adelgren et al.[32] allowed the observation of energy-deposition effects on a spherical shock wave at Mach 3.45. The region of laser heating is approximately a point source; however, it is somewhat elongated along the direction of laser-pulse propagation, which occurs transverse to the tunnel's airflow. (The beam enters from the side of the tunnel.) The resultant heating can effectively be approximated as a point source, whose evolution as an expanding spherical shock wave has been extensively treated.[38,39] The main signature of this

expansion is the spherical shock wave driving a high-density/high-pressure wave outward, leaving a hot, low-density bubble in the center. This low-density bubble expands to a point and then stops, as the shock wave continues outward and weakens.

To investigate what we believed to be a more effective cylindrical geometry, an incremental investigation was performed in 2000, in which a line of gas was heated, to demonstrate the feasibility of attaining this geometry. This investigation was performed in quiescent air, as well as along a streamline ahead of a conical model in a classroom supersonic wind tunnel at the University of Arizona. The geometry was similar to that seen in our numerical display in Fig. 1. Although the flow was not thoroughly characterized, the results of this investigation (to be published elsewhere) indicated drag reduction and shock mitigation through sudden heat addition along a streamline ahead of a shock wave. The method was inferred to result in significant energy savings and is anticipated to apply to both streamlined and bluff bodies. This demonstrated the potential for control and was documented and modeled to some degree in Refs. 41 and 42.

In terms of a supersonic vehicle, very little air is pushed out of a vehicle's path with a point-heating geometry. Nearly half of the gas expands toward the vehicle and impinges head on with the vehicle's shock wave, while the other half moves away from the vehicle, only to be "caught up to" and absorbed by the vehicle's shock wave. Georgievsky and Levin. have documented these inefficiencies in Ref. 43. In contrast, for the case of sudden line heating, nearly all of the cylindrically expanding gas is pushed out of the way of the vehicle's path. In fact, a long-lived reduction in density is observed surrounding the heated path, well after the gas is initially heated, similar to that simulated inviscidly by Soloviev et al.[44] It is along this low-density core that the vehicle will travel.

Once the vehicle has fully exploited a heated path (core), another violently heated path can be created, resulting in a repetition rate, which is dictated roughly by the vehicle's size and speed, as well as the length of the heated core. To scale the method up beyond a single heated path, arrays of individual heating elements can be implemented. The energy deposition from these arrays can be phased to maintain strong outward gas expansion, tailored to the size and speed of the vehicle.

III.   Numerical Results

To account for the complex dynamics and shock/shock interactions inherent in this problem, a novel modeling formalism was required to properly simulate the shock dynamics. This method was a multidomain WENO high-order finite difference method in which interpolation is employed at subdomain interfaces. WENO schemes were originally designed based on the successful essentially nonoscillatory (ENO) schemes by Harten et al.[45] Finite volume WENO schemes have been constructed by Liu et al.[46] for a third-order version in one space dimension, by Friedrichs[47] and Hu and Shu[48] for second-, third-, and fourth-order versions for two-dimensional general triangulations, and by Shi et al.[49] for high-order versions containing negative linear weights. Finite difference WENO schemes have been constructed by Jiang and Shu[50] for the third- and fifth-order versions in multispace dimensions with a general framework for the design of the smoothness indicators and nonlinear weights and by Balsara and Shu[51] for very high-order (between 7 and 11) versions. Recently, Sebastian and Shu[1] constructed a multidomain fifth-order WENO finite difference scheme of which the numerical simulations described in this paper comprise.

A.   Multidomain WENO Finite Difference Algorithm

Both ENO and WENO use the idea of adaptive stencils in the reconstruction procedure based on the local smoothness of the numerical solution to automatically achieve high-order accuracy and the nonoscillatory property near discontinuities. ENO uses just one (optimal in some sense) out of many candidate stencils when doing the reconstruction. WENO, on the other hand, uses a convex combination of all of the candidate stencils, each being assigned a nonlinear weight, which depends on the local smoothness of the numerical solution based on that stencil. WENO improves

on ENO in robustness, better smoothness of fluxes, better steady-state convergence, better provable convergence properties, and more efficiency.

There are two types of WENO schemes, namely, the finite volume schemes and the finite difference schemes. In one spatial dimension, the finite volume schemes and the finite difference schemes are equivalent, both in numerical resolution and accuracy and in complexity of coding and CPU timing. For multispatial dimensions, however, they are no longer equivalent. Although finite difference schemes are still very simple to code and fast to compute (essentially only one or more outside "do loops" are needed to change a one dimensional finite difference code to multidimensions), the finite volume code becomes much more complicated and costly. The multidomain framework employed in our numerical simulations served multiple purposes. To utilize the speedier finite difference framework in this two-dimensional problem, it became necessary to divide the larger domain into three smaller subdomains to allow for the computation of the complex geometry around the cone-shaped vehicle in flight. These subdomains can be observed graphically in the figures to follow.

The drawback to using this finite difference scheme over several subdomains is that conservation error is necessarily introduced because interpolation in any manner is nonconservative if it is not based on cell averages. Much time was spent on this "drawback" during the development of the method. Most importantly, it has been proved[1] that under suitable assumptions interpolation does not produce $\mathcal{O}(1)$ conservation error. In fact, the method is essentially conservative in that the conservation error reduces with reduction in mesh size. Also, many numerical investigations have shown that full high-order accuracy is maintained across the global domain, and the essentially nonoscillatory results are also maintained even though interpolation is employed at subdomain interfaces. Furthermore, a thorough grid refinement (convergence) study was employed in Ref. 1 showing the accuracy of the multidomain WENO method for both one- and two-dimensional standard test cases. In addition, we studied the convergence of our method on the specific computations of this current study by comparing the results of one specific case with three different mesh sizes. It is clear then from the results displayed in our numerical simulation summary in Table 2 that the use of the specific mesh sizing as described in the following section is satisfactory and gives reliable results.

B. Axisymmetric Euler System in Three Dimensions

To compute the type of flow we have described thus far in this paper, the flow is assumed to be governed by the axisymmetric Euler equations in three dimensions. Because the equations are axisymmetric, they reduce to a two-dimensional Euler system with an extra equation and some forcing terms on the right-hand side. To be specific, the three-dimensional axisymmetric Euler equations reduce to the following two-dimensional system:

$$
\begin{bmatrix} \rho \\ \rho u_x \\ \rho u_r \\ \rho u_\theta \\ E \end{bmatrix}_t + \begin{bmatrix} \rho u_x \\ \rho u_x^2 + p \\ \rho u_r u_x \\ \rho u_\theta u_x \\ u_x(E + p) \end{bmatrix}_x + \begin{bmatrix} \rho u_r \\ \rho u_x u_r \\ \rho u_r^2 + p \\ \rho u_\theta u_r \\ u_r(E + p) \end{bmatrix}_r = \begin{bmatrix} \dfrac{\rho u_r}{r} \\ \dfrac{\rho u_x u_r}{r} \\ \dfrac{\rho \left(u_r^2 - u_\theta^2\right)}{r} \\ \dfrac{2\rho u_\theta u_r}{r} \\ \dfrac{u_r(E + p)}{r} \end{bmatrix}
\tag{1}
$$

where E is the total energy:

$$
E = p/(\gamma - 1) + \tfrac{1}{2}\rho \left(u_x^2 + u_r^2 + u_\theta^2\right)
\tag{2}
$$

It is particularly important here to note that the pressure, density, and temperature are nondimensionalized with respect to their mean upstream values P_1, ρ_1, and T_1, respectively, and are related by the ideal-gas law

$$
p = \rho T
\tag{3}
$$

The velocity is scaled by the reference velocity $c^* = (RT_1)^{1/2}$, where R is the gas constant for air, related to the upstream mean sound speed $c_1 = \gamma^{1/2}c^*$. If M_1 is the upstream Mach number in a frame of reference in which the mean shock is stationary, then $M_1 = |U_1|/\gamma^{1/2}$. This nondimensionalization is pertinent to the results of our numerical experiments and will be explained later.

What was desired when the work on this problem began was to be able to show that a compelling advantage in shock mitigation and drag reduction would exist if one could suddenly deposit heat (i.e., energy) along a streamline ahead of a shock wave. To numerically study this question, the research has focused on studying axisymmetric supersonic flow over a cone. The cone approximates a vehicle in supersonic flight. With this framework in mind, the first step was to set up the global domain and divide it into appropriate subdomains in order to be able to make use of the multidomain WENO finite difference method. It was clear that a choice of three subdomains was the minimum requirement. Also, because the problem is axisymmetric, it was only necessary to solve the equations in the upper half of the (x, r) plane. The figures that follow provide a full (x, r)-plane view, but these were not necessary to compute. They were simply constructed from the upper half-plane results using the axisymmetry.

The first step was to acquire steady-state solutions of the supersonic flow over cones with varying half-angles. (This is the angle made by the conical surface with the cone axis.) We chose to study cones with half-angles of 45, 30, and 15 deg. Supersonic flows with Mach numbers of 2, 4, 6, and 8 were all computed. These steady-state solutions were utilized as the initial conditions in the low-density-core studies. For brevity, these steady-state conditions are shown only for a half-angle of 45 deg, in flows with Mach numbers 2 and 4 in Fig. 2. Note the different scales for the x and r axes.

If the subdomains are numbered 1–3 from left to right, the number of mesh points for the 45-deg half-angle cone chosen in each subdomain was such that $\Delta x = \Delta r = 1/30$ in subdomain 1 and $\Delta x = \Delta r = 1/60$ in subdomains 2 and 3. The number of mesh points in subdomains 2 and 3 for the 30- and 15-deg half-angle cones was adjusted so that the aspect ratio of the interpolations at the subdomain boundaries remained similar to that for the 45-deg half-angle cone. The top boundary of each subdomain was taken to be freestream flow. The left boundary of subdomain 1 was taken to be free inflow, and the right boundary of subdomain 3 was taken to be free outflow. The bottom boundaries of all three of the subdomains were reflective. This is clear for the portions of the boundaries

Table 2 Convergence study to determine appropriate mesh spacing for the numerical experiments

| Mesh	LDCR	ES	% Change[a]
Coarse[b]	$\frac{1}{4}R$	12.494	——
	$\frac{1}{2}R$	21.282	——
	$\frac{3}{4}R$	26.750	——
	R	29.432	——
Fine[c,d]	$\frac{1}{4}R$	14.742	17.99
	$\frac{1}{2}R$	25.123	18.05
	$\frac{3}{4}R$	29.337	9.67
	R	32.137	9.19
Finest[e]	$\frac{1}{4}R$	14.707	0.23
	$\frac{1}{2}R$	25.518	1.57
	$\frac{3}{4}R$	29.096	0.82
	R	32.565	1.33

[a]The percentage change observed in the energy savings value in changing from the coarse mesh to the fine mesh is much greater than the percentage change observed in going from the fine mesh to the finest mesh.
[b]The coarse mesh sizing corresponds to $\Delta x = \Delta y = \frac{1}{15}$ on grid 1 and $\Delta x = \Delta y = \frac{1}{30}$ on grids 2 and 3.
[c]The fine mesh sizing corresponds to $\Delta x = \Delta y = \frac{1}{30}$ on grid 1 and $\Delta x = \Delta y = \frac{1}{60}$ on grids 2 and 3.
[d]This experiment led us to the conclusion that the results obtained from the fine mesh are reliable and appropriately balance accuracy vs computer run time.
[e]The finest mesh sizing corresponds to $\Delta x = \Delta y = \frac{1}{45}$ on grid 1 and $\Delta x = \Delta y = \frac{1}{90}$ on grids 2 and 3.
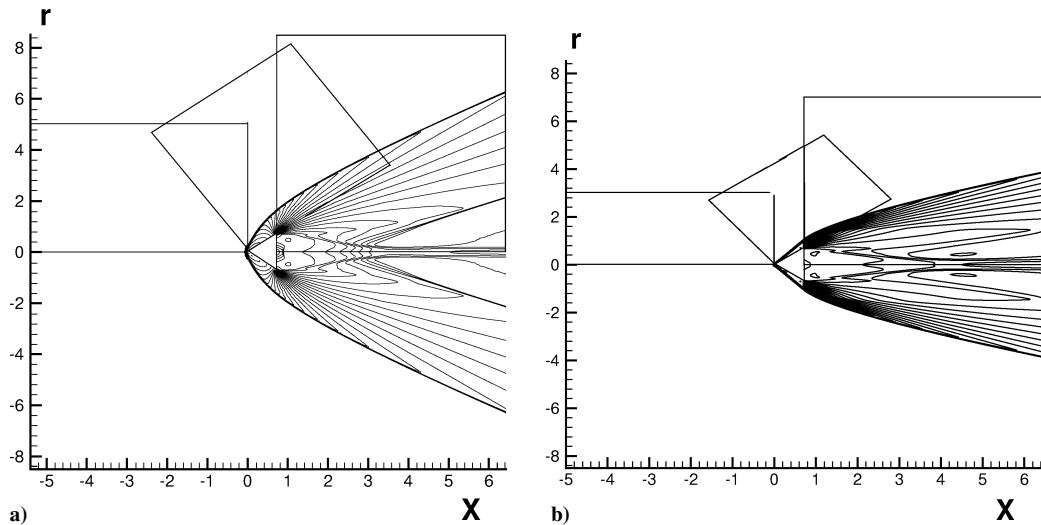
Fig. 2 Inviscid steady-state axisymmetric flow over a 45-deg half-angle cone is demonstrated for two different Mach numbers: a) 2 and b) 4. The computational subdomains are indicated by the "drawn in" rectangles. Both graphs give 30 equally spaced density contours chosen appropriately to include all values computed. The results are displayed after 52,000 time steps and compared visually as well as in the L_1 norm in time to ensure they indeed represent the steady-state flow.

that lie along the cone. It is also correct in axisymmetric flow with an open bottom boundary lying along the x axis such as those of subdomains 1 and 3. This is because the u_r component of velocity opposes itself above and below the x axis, whereas the u_x and u_θ components of velocity are the same both above and below the x axis.

Using this described technique at the specified Mach numbers and cone angles, it was expected that we would be able to accurately calculate the base pressure. To verify this, we compared the steady-state drag on our cones against analytical inviscid cone solutions after subtracting the commonly used and widely verified approximation to the base pressure coefficient $-1/M^2$ (Ref. 52). The inviscid cone solutions yield a constant pressure along the conical surface of the cone. Because an expansion wave/fan propagates toward the cone axis after the flow crosses the cone edge, truncating the infinite cone results in a lower pressure at the cone base. The reduced pressure serves as a suction to draw the cone backward and yields a greater total drag on the cone than if accounting only for the pressure on the conical face. To establish the accuracy of our total drag values (both with and without energy deposition), it was important for us to verify our steady-state results in undistorted flow against the analytical results, corrected using the experimentally verified $-1/M^2$ approximation for the base pressure coefficient. As can be seen in Table 1, our results for a cone with a 30-deg half-nose angle agree exceptionally well with the commonly accepted inviscid results of Sims from NASA Marshall Space Flight Center in Ref. 53.

We assumed that the physical method of opening up a low-density core was to instantaneously increase the temperature and pressure of the gas in a thin, long region ahead of the cone. The best way to impose this numerically was to instantaneously deposit energy along the cone axis ahead of the cone. Thus, once the steady-state flow initial conditions were computed, it was necessary to determine the amount of energy to deposit along the cone axis to open up low-density cylindrical cores of various radii. Because the equations are nondimensionalized, this was most easily determined through numerical simulation, testing different amounts of energy deposits. This energy was deposited along a line of length $5L$, where L is the length of the cone from the base to the tip. This length was chosen as it is sufficient to reach a relatively constant low-drag state. The deposited energy created low-density cores of $\frac{1}{4}R$, $\frac{1}{2}R$, $\frac{3}{4}R$, and R, where R is the radius of the cone's base. Because of the reflective boundary condition at the bottom of subdomain 1 where the energy was applied, it was not truly applied along a line. This line in reality had a thickness of radius Δr because the first mesh points must be at a distance of $\Delta r/2$ from the line $x = 0$ to utilize the reflective boundary condition. The amount of energy required was indeed

proportional to the square of the radius of the low-density core it opened. Thus, once the amount of energy $E_{1/4R}$ required to open up a low-density core of radius $\frac{1}{4}R$ was determined through numerical experiment, the other energy amounts were simply $4\,E_{1/4R}$, $9\,E_{1/4R}$, and $16\,E_{1/4R}$, respectively.

For the nondimensional axisymmetric Euler equations and the total energy equation just described, we achieved four different upstream initial conditions corresponding to Mach numbers 2, 4, 6, and 8. For each case, we achieved the upstream initial condition by setting $\rho = 1$, $p = 1$, and $u_x = M \times \sqrt{\gamma}$ with $u_r = u_\theta = 0$. The initial upstream energy is then easily calculated from these values using the total energy equation. Once these conditions were prescribed, we allowed the equations to evolve on our prescribed domain for a very long time, precisely 52,000 time steps, which gave us a difference in the flow variables of 10^{-5} between successive time steps, thereby indicating a satisfactory steady state had been achieved.

Finally, to open up a low-density core, an instantaneous deposition of energy was made over a fixed length of $5L$ as just described. The amount of energy necessary to be deposited is not related to the upstream initial conditions in any way other than we ensured it was deposited far enough ahead of the cone tip to be open to the desired amount by the time the core reached the cone tip. The energy deposition required for the various low-density core radii was determined through numerical experiment. It was observed to agree with Plooster's result that the energy required was proportional to the square of the desired low-density core radius, constants notwithstanding. The exact nondimensional energy deposition (compared to the nondimensional initial energy conditions just described) and the corresponding instantaneous increase in temperature and pressure of the gas in this thin, long region are given in Table 3. Examination of these values is based on the fact that they are nondimensionalized with the initial temperature, density, and pressure conditions all being assigned the value 1.0. Equations (2) and (3) describe the relationship between energy, pressure, density, and temperature. They can be used to easily verify the resulting instantaneous increases in pressure and temperature that are assumed based on the instantaneous energy depositions made in our numerical experiments.

Figure 3 gives the graphical results from only one of the many numerical simulations performed. The Mach 2 results, over a cone of 45-deg half-angle, provide the most dramatic graphical results, and only these are presented in the interest of brevity. Each of the steady-state flows was subjected to an instantaneous line deposition of energy as just described. The deposition occurred just far enough ahead of the cone tip so that the low-density cylindrical core created by this energy was open to its full radius as the front of the core

Table 3   Initial energy deposition amounts to open up low-density cores of various radii for various Mach numbers

Mach	LDCR[a]	IUE[b]	EGE[c,d]	PTGE[e]	LV45	TLE45	LV30	TLE30	LV15	TLE15
2	$\frac{1}{4}R$	5.3	88	35	0.003	0.272	0.005	0.470	0.012	1.013
	$\frac{1}{2}R$	5.3	352	141	0.003	1.086	0.005	1.881	0.012	4.053
	$\frac{3}{4}R$	5.3	792	317	0.003	2.444	0.005	4.232	0.012	9.120
	R	5.3	1408	563	0.003	4.344	0.005	7.524	0.012	16.213
4	$\frac{1}{4}R$	13.7	88	35	0.003	0.272	0.005	0.470	0.012	1.013
	$\frac{1}{2}R$	13.7	352	141	0.003	1.086	0.005	1.881	0.012	4.053
	$\frac{3}{4}R$	13.7	792	317	0.003	2.444	0.005	4.232	0.012	9.120
	R	13.7	1408	563	0.003	4.344	0.005	7.524	0.012	16.213
6	$\frac{1}{4}R$	27.7	88	35	0.003	0.272	0.005	0.470	0.012	1.013
	$\frac{1}{2}R$	27.7	352	141	0.003	1.086	0.005	1.881	0.012	4.053
	$\frac{3}{4}R$	27.7	792	317	0.003	2.444	0.005	4.232	0.012	9.120
	R	27.7	1408	563	0.003	4.344	0.005	7.524	0.012	16.213
8	$\frac{1}{4}R$	47.3	88	35	0.003	0.272	0.005	0.470	0.012	1.013
	$\frac{1}{2}R$	47.3	352	141	0.003	1.086	0.005	1.881	0.012	4.053
	$\frac{3}{4}R$	47.3	792	317	0.003	2.444	0.005	4.232	0.012	9.120
	R	47.3	1408	563	0.003	4.344	0.005	7.524	0.012	16.213

[a]LDCR is the low-density core radius in terms of the radius of the base of the cone R.
[b]IUE is the initial upstream steady-state energy necessary for a flow with the corresponding Mach number.
[c]EGE is the instantaneous energy deposited per grid element to open up the low-density core.
[d]EGE multiplied by the LV (line volume) of the line upon which the energy is deposited gives us the TLE (total line energy) deposited to open up each low-density core corresponding to the size of the cone (which is different for each cone tip half-angle to keep the aspect ratio of the interpolations required at each subdomain interface the same).
[e]PTGE is the instantaneous pressure and temperature increases that result from the instantaneous energy deposition.
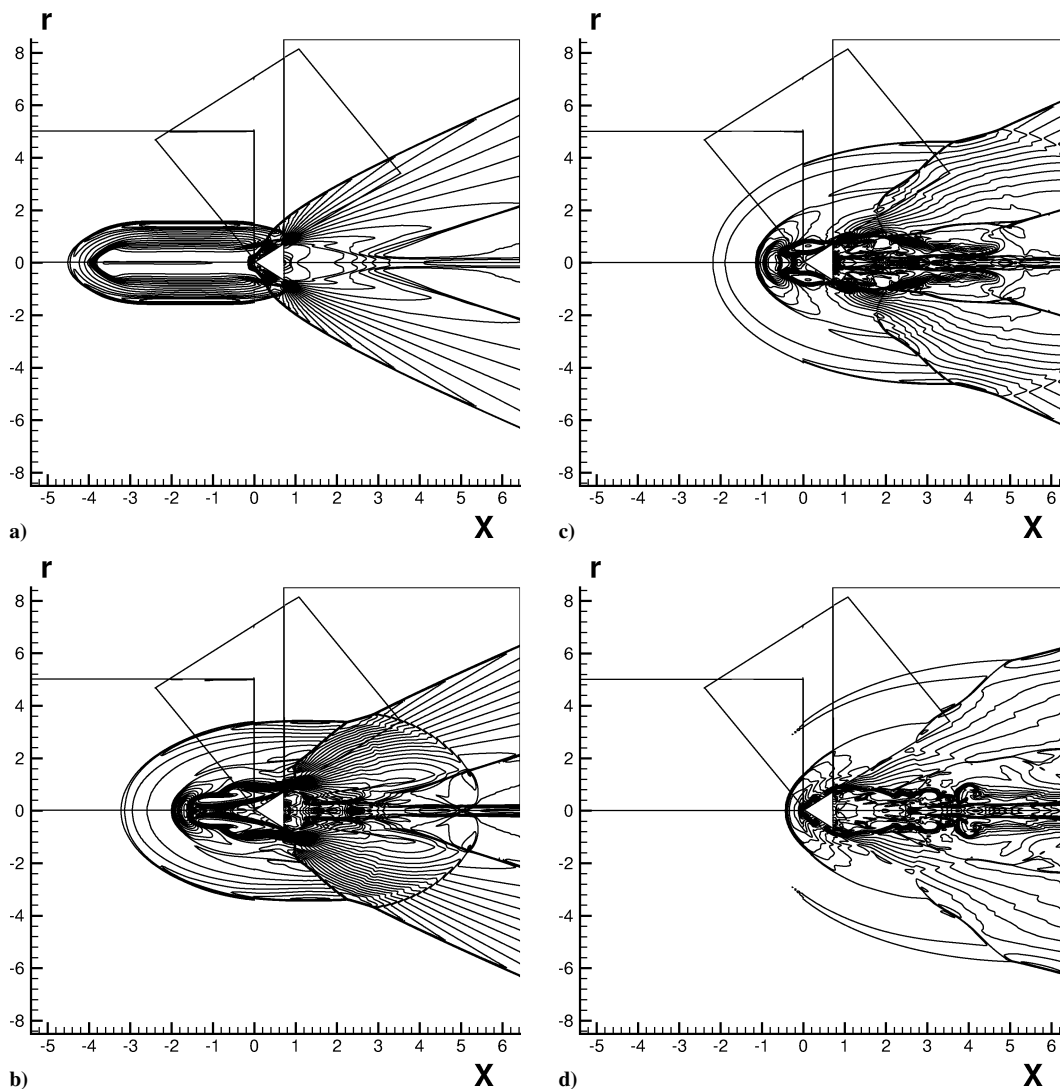
Fig. 3   Low-density core problem for Mach 2 flow over a cone. The cone half-angle is 45 deg over which a low-density core of radius = R_{cone} is fully opened when it reaches the cone tip and remains open as it passes by the cone. The snapshots are taken at specific instants in time, namely, when a) the leading edge of the low-density core was at the cone tip, b) the middle of the core would be at the cone tip, c) the trailing edge of the core would be at the cone tip, and d) the core would have traveled completely past the cone by one full unit in the x direction.

reached the cone tip. Based on a determination of how much distance would be covered by the low-density core if it were traveling in a freestream flow without the cone as an obstacle, density contour snapshots were then taken at specific times. These times were selected to view the contours when 1) the leading edge of the low density core was at the cone tip; 2) the middle of the core would be at the cone tip; 3) the trailing edge of the core would be at the cone tip; and finally, 4) the core would have traveled completely past the cone by one full unit in the x direction if it would have been in freestream flow only. Contour plots are presented in Fig. 3 of a low-density core opened to a full cone radius R in the Mach 2 flow. The contour levels were chosen appropriately to include all values of density computed.

Pressure contours will not be shown here, as they do not contribute much additional insight. It is clear from the pictured density contour plots that shock mitigation occurs. At all four Mach numbers, a comprehensive assessment was also performed of the resulting drag force on each cone shape, for each of the low-density core radii. At every time step, the drag, that is, pressure force per unit area, on the cone was computed as

$$D_{\text{tot}} = D_{\text{cs}} - D_{\text{cb}} = 2\pi \left[\sum_{i_{\text{cs}}} \sin(\theta) r_i p_i - \sum_{j_{\text{cb}}} r_j p_j \right] \quad (4)$$

Table 4 Numerical simulation results for the 45-deg half-angle cone

Mach SSD[a]	LDCR[b]	ECC TCE[c,d]	ES % ESE[e,f]	LDV[g]	% DR[h]
2 5.845	$\frac{1}{4}R$	0.077 0.272	14.742 5319.85	1.080	81.52
	$\frac{1}{2}R$	0.307 1.086	25.123 2213.35	0.736	86.94
	$\frac{3}{4}R$	0.691 2.444	29.337 1100.37	0.611	89.55
	R	1.229 4.344	32.137 639.80	0.219	96.25
4 19.615	$\frac{1}{4}R$	0.077 0.272	3.953 1355.87	17.748	9.52
	$\frac{1}{2}R$	0.307 1.086	40.735 3650.91	7.710	60.69
	$\frac{3}{4}R$	0.691 2.444	74.517 2949.49	2.786	85.80
	R	1.229 4.344	83.251 1816.38	1.669	91.49
6 41.640	$\frac{1}{4}R$	0.077 0.272	8.219 2927.07	37.429	10.11
	$\frac{1}{2}R$	0.307 1.086	37.931 3392.68	28.598	31.32
	$\frac{3}{4}R$	0.691 2.444	126.707 5085.26	6.060	85.45
	R	1.229 4.344	166.683 3736.92	2.553	93.87
8 72.395	$\frac{1}{4}R$	0.077 0.272	13.712 4950.39	65.091	10.09
	$\frac{1}{2}R$	0.307 1.086	59.674 5394.85	49.694	31.36
	$\frac{3}{4}R$	0.691 2.444	161.107 6493.02	22.964	68.28
	R	1.229 4.344	268.770 6086.88	3.750	94.82

[a]SSD is the steady-state drag on the cone.
[b]LDCR is the low-density core radius in terms of the radius of the base of the cone R.
[c]ECC is the nondimensionalized energy per length required to create the core.
[d]TCE is the total amount of energy required to create the core.
[e]ES is the overall energy saved as the cone passed through the low-density core and returned to steady state.
[f]% ESE is the percentage energy savings "efficiency," i.e., the ratio (in percent) of [overall energy saved (minus the energy expended to create the core)] to (overall energy expended to create the low-density core).
[g]LDV is the lowest drag value experienced by the cone as it passed through the low-density core.
[h]% DR is the percentage of drag reduction experienced with the lowest drag value as compared to the steady-state drag.

Here, $\sum_{i_{\text{cs}}}$ indicates to sum over all grid elements lying along the side of the cone. Likewise, $\sum_{j_{\text{cb}}}$ indicates to sum over all grid elements along the base of the cone. θ is the cone half-angle. The r_i and r_j indicate the radius of the cone at the specific grid elements. Likewise, the p_i and p_j are the pressures at each specific grid element. Because the flow is axisymmetric, only the pressure force in the x direction is not canceled by an equal and opposite force on the opposing face of the cone. Additionally, the pressure on the base of the cone "presses" in a direction opposite to the freestream flow; thus, these components subtract from the overall drag. Finally, the factor of $2\pi r$ is an approximate measure of the surface area over which that component of the drag force (pressure) is acting. Figure 4 shows the drag reduction that was obtained as a low-density core of full cone radius R was opened ahead of a cone in Mach 2 flow. This drag-reduction graph accompanies Fig. 3 in which four density contour plots are shown at various times as the cone passes through the low-density core.

C. Numerical Simulation Summary

To facilitate comparison to experiment and theory, we chose to model the cones at zero angle of attack. For each of the different cone angles, we maintained the same base diameter. This resulted in longer cones for smaller half-angles. To obtain a more complete picture of the low-density core's interaction with each cone, we always generated a heated core that was five times as long as the cone. As stated earlier, this length was chosen as it is sufficient to reach a

Table 5 Numerical simulation results for the 30-deg half-angle cone

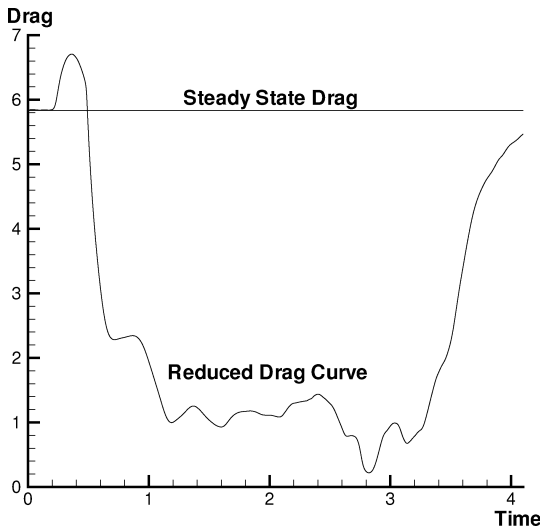| Mach SSD[a]	LDCR[b]	ECC TCE[c,d]	ES % ESE[e,f]	LDV[g]	% DR[h]
2 3.842	$\frac{1}{4}R$	0.077 0.470	4.844 930.00	2.861	25.54
	$\frac{1}{2}R$	0.307 1.881	15.407 719.04	1.077	71.97
	$\frac{3}{4}R$	0.691 4.232	26.967 537.17	0.827	78.49
	R	1.229 7.524	33.111 340.06	0.756	80.32
4 10.871	$\frac{1}{4}R$	0.077 0.470	4.924 946.99	9.882	9.09
	$\frac{1}{2}R$	0.307 1.881	32.750 1641.00	4.828	55.58
	$\frac{3}{4}R$	0.691 4.232	52.815 1147.88	2.565	76.40
	R	1.229 7.524	59.625 692.44	1.813	83.32
6 22.270	$\frac{1}{4}R$	0.077 0.470	8.305 1665.98	20.282	8.93
	$\frac{1}{2}R$	0.307 1.881	45.933 2341.81	13.762	38.21
	$\frac{3}{4}R$	0.691 4.232	106.668 2420.27	4.603	79.33
	R	1.229 7.524	124.857 1559.38	2.609	88.28
8 38.534	$\frac{1}{4}R$	0.077 0.470	14.661 3017.37	34.961	9.27
	$\frac{1}{2}R$	0.307 1.881	67.221 3473.47	25.294	34.36
	$\frac{3}{4}R$	0.691 4.232	178.350 4113.92	8.726	77.35
	R	1.229 7.524	212.407 2722.94	3.678	90.45

[a]SSD is the steady-state drag on the cone.   [b]LDCR is the low-density core radius in terms of the radius of the base of the cone R.   [c]ECC is the nondimensionalized energy per length required to create the core.   [d]TCE is the total amount of energy required to create the core.   [e]ES is the overall energy saved as the cone passed through the low-density core and returned to steady state.   [f]% ESE is the percentage energy savings efficiency, i.e., the ratio (in percent) of [overall energy saved (minus the energy expended to create the core)] to (overall energy expended to create the low-density core).   [g]LDV is the lowest drag value experienced by the cone as it passed through the low-density core.   [h]% DR is the percentage of drag reduction experienced with the lowest drag value as compared to the steady-state drag.

Table 6 Numerical simulation results for the 15-deg half-angle cone

| Mach SSD[a]	LDCR[b]	ECC TCE[c,d]	ES % ESE[e,f]	LDV[g]	% DR[h]
2	$\frac{1}{4}R$	0.077	1.792	1.562	9.77
1.731		1.013	76.87		
	$\frac{1}{2}R$	0.307	6.217	1.040	39.93
		4.053	53.38		
	$\frac{3}{4}R$	0.691	12.923	0.588	66.04
		9.120	41.70		
	R	1.229	16.341	0.344	80.15
		16.213	0.79		
4	$\frac{1}{4}R$	0.077	2.725	3.523	7.28
3.800		1.013	168.91		
	$\frac{1}{2}R$	0.307	15.535	2.392	37.05
		4.053	283.28		
	$\frac{3}{4}R$	0.691	24.713	1.717	54.82
		9.120	170.99		
	R	1.229	30.613	1.223	67.83
		16.213	88.82		
6	$\frac{1}{4}R$	0.077	5.257	5.885	8.90
6.460		1.013	418.81		
	$\frac{1}{2}R$	0.307	29.859	3.593	44.38
		4.053	636.68		
	$\frac{3}{4}R$	0.691	48.692	2.085	67.73
		9.120	433.93		
	R	1.229	58.473	1.254	80.59
		16.213	260.66		
8	$\frac{1}{4}R$	0.077	8.803	9.471	9.34
10.447		1.013	768.77		
	$\frac{1}{2}R$	0.307	39.057	6.501	37.77
		4.053	864.64		
	$\frac{3}{4}R$	0.691	90.126	2.933	71.93
		9.120	888.26		
	R	1.229	103.846	1.506	85.58
		16.213	540.53		

[a]SSD is the steady-state drag on the cone.
[b]LDCR is the low-density core radius in terms of the radius of the base of the cone R.
[c]ECC is the nondimensionalized energy per length required to create the core.
[d]TCE is the total amount of energy required to create the core.
[e]ES is the overall energy saved as the cone passed through the low-density core and returned to steady state.
[f]% ESE is the percentage energy savings efficiency, i.e., the ratio (in percent) of [overall energy saved (minus the energy expended to create the core)] to (overall energy expended to create the low-density core).
[g]LDV is the lowest drag value experienced by the cone as it passed through the low-density core.
[h]% DR is the percentage of drag reduction experienced with the lowest drag value as compared to the steady-state drag.

Fig. 4   Drag reduction obtained as a cone in Mach 2 flow passes through a low-density core of full cone radius R is shown. The core causes a momentary increase in drag as its expanding shock wave hits the cone; however, the drag is shown to significantly decrease for a sustained time period as the cone passes through the low-density core.

relatively constant low-drag state. Every numerical experiment conducted reached a relatively steady low-drag state; thus, it was not crucial to our results to conduct experiments with other low-density core lengths. As a result, the pertinent value, against which we show some graphs and summarizing tables, is the energy/length deposited in the flow (which is aligned with Plooster's model).

To summarize the numerical results at a glance, Table 4 gives the results for the cone with 45-deg half-angle, Table 5 gives the results for the cone with 30-deg half-angle, and Table 6 gives the results for the cone with 15-deg half-angle.
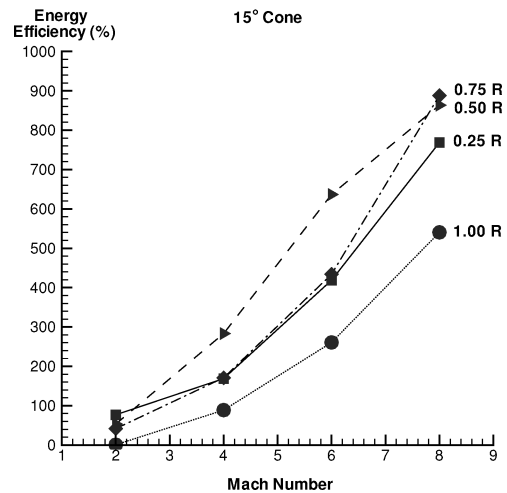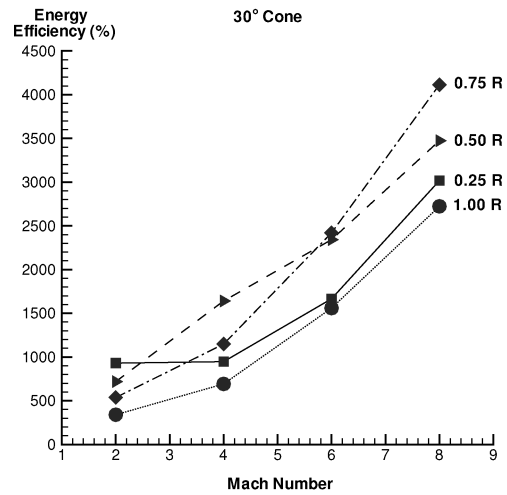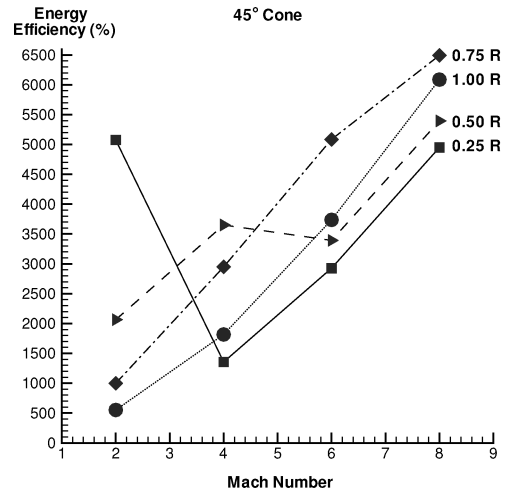
Fig. 5   Display of the overall energy savings efficiency percentage of creating a low-density core for each of the supersonic flows computed and each of the cores created.

As mentioned earlier, in addition to the comprehensive convergence study of the multidomain WENO algorithm completed in Ref. 1, we also computed the Mach 2 case with three different mesh sizes. First, we computed the Mach 2 case with a mesh consisting of enough points to satisfy $\Delta x = \Delta y = 1/15$ on grid 1 and $\Delta x = \Delta y = 1/30$ on grids 2 and 3. Then, we computed the Mach 2 case with a mesh consisting of enough points to satisfy $\Delta x = \Delta y = 1/30$ on grid 1 and $\Delta x = \Delta y = 1/60$ on grids 2 and 3. Finally, we computed this case with a mesh consisting of enough

points to satisfy $\Delta x = \Delta y = 1/45$ on grid 1 and $\Delta x = \Delta y = 1/90$ on grids 2 and 3. The results of these computations can be found in Table 2. They indicate that the mesh we chose to use gives us no more than 1.57% error in comparison to a more refined mesh.

To give a complete visual depiction of our results, the following graphs are also shown. In Fig. 5, we plot the energy savings efficiency experienced when creating each of the four different low-density cores ($\frac{1}{4}R$, $\frac{1}{2}R$, $\frac{3}{4}R$, R) in each of the supersonic flows considered (Mach 2, 4, 6, 8). Likewise, in Fig. 6, we display the maximum drag reduction obtained when the cone passes through the low-density core. "Energy savings" is the difference between the energy expended to maintain a constant velocity with and without heating ahead of the cone. This energy expenditure is calculated by integrating the product of the drag and velocity over the amount of time that the core perturbs the steady-state flow. "Energy savings efficiency" is the energy savings (minus the amount of energy invested to achieve this savings) divided by the amount of energy invested to achieve this savings. Both drag reduction and energy savings efficiency are shown as percentages to avoid confusion.

In Fig. 7, a rough three-dimensional view of the Energy savings efficiency is presented. Viewing the data as a surface helps visualize the existence of potential "sweet spots," exhibiting maximal benefit. Their localized nature demonstrates the utility of mapping
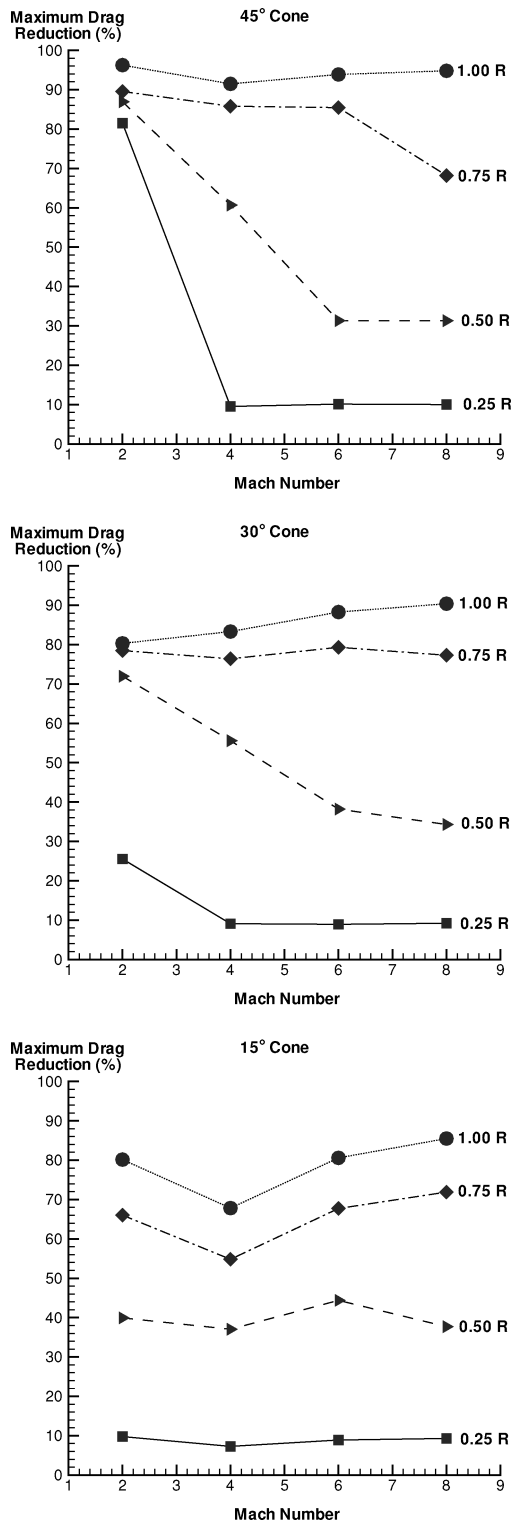

Fig. 6   Display of the maximum drag-reduction percentage as a result of creating a low-density core for each of the supersonic flows computed and each of the cores created.
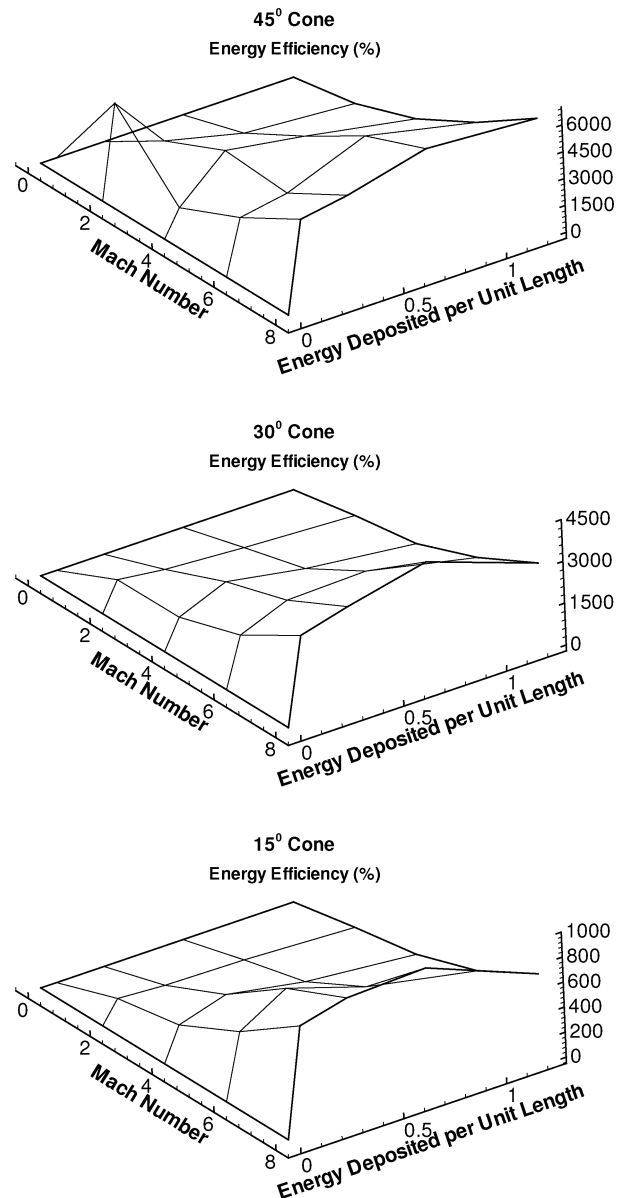

Fig. 7   Three-dimensional views of the overall energy savings efficiency (as a percentage) obtained for the three cone half-angles.

the "landscape" with greater resolution by performing runs at Mach numbers and energy deposition values intermediate to those already plotted.

Our next step in the supersonic/hypersonic regimes will be to experimentally demonstrate and characterize the described method in a clean wind tunnel with excellent high-resolution diagnostics. Experimental data on cones will allow us to further validate our computational methods, which can then be used to investigate optimized vehicle designs and to make scale models for further testing and advances in our wind-tunnel experiments. Additional areas for future investigation are to explore optimal geometry and frequency of energy deposition for flow control and drag reduction[54,55]; use energy deposition to mitigate an adverse flow condition, as well as reduce drag; and develop dynamic, data-driven control for energy deposition to optimize drag reduction and shock mitigation.

IV. Conclusions

Long columns of energy, deposited ahead of a vehicle, significantly reduce drag in supersonic/hypersonic regimes. The expansion of a cylindrical shock wave from the line of deposited energy results in a long, low-density column of air ahead of the vehicle. This column of low-density air interacts with the vehicle's shock wave, providing a low-density channel, along which the high-pressure gas in front of the vehicle can escape, and along which the vehicle can travel with greatly reduced wave drag. Having compared this method to energy deposition at a "point" ahead of the shock wave, we have numerically demonstrated a far greater benefit for deposition along lines, which are aligned with the vehicle's direction of motion.

As much as a 96% reduction in drag was observed as a direct result of the energy deposition. The drag reduction is also economically favorable, with a "return on invested energy" as high as 6500%. Different amounts of deposited energy (yielding different radii low-density columns) yield the highest energy efficiency for different Mach numbers and cone half-angles.

We emphasize here that we have chosen to conduct numerical simulations of inviscid flow over a sharp-tipped cone [see Eq. (1) and Fig. 2]. Our method(s) of adding energy to the flow generally involve ionization and radiation; however, we are considering no real-gas effects, such as vibration, dissociation, and ionization. As such, we considered only the amount of energy coupled into the flow. Furthermore, our primary goal was to determine the reduction in wave drag provided by the described energy deposition technique. As such, we did not incorporate an artificial boundary layer to investigate skin friction. As a result, another clear extension of our work will be to use the full Navier–Stokes equations. In dynamically calculating the drag throughout the course of our drag-reduction technique, both the lower pressure on the cone face and a higher pressure on the cone base caused by the low-density core contribute to the observed lower drag. This will be accurately detailed once we modify our code to incorporate the full Navier–Stokes equations.

Lastly, the proposed drag-reduction method cannot rely on a single energy pulse as we have currently modeled. The pulses have to be repeated at a high rate. Questions concerning optimal repetition rate for best overall time-averaged drag reduction will have to be answered. Therefore, future work will also include our modeling of repeated energy pulses.

References

[1]Sebastian, K., and Shu, C.-W., "Multi Domain WENO Finite Difference Method with Interpolation at Sub-Domain Interfaces," *Journal of Scientific Computing*, Vol. 19, No. 1–3, 2003, pp. 405–438.

[2]Guy, Y., McLaughlin, T. E., and Morrow, J. A., "Blunt Body Wave Reduction by Means of a Standoff Spike," AIAA Paper 2001-0888, Jan. 2001.

[3]Nemchinov, I. V., Artem'ev, V. I., Bergel'son, V. I., Khazins, V. M., Orlova, T. I., and Rybakov, V. A., "Rearrangement of the Bow Shock Shape Using a 'Hot Spike,'" *Shock Waves*, Vol. 4, July 1994, pp. 35–40.

[4]Kandebo, S. W., "Air Spike Could Ease Hypersonic Flight Problems," *Aviation Week and Space Technology*, Vol. 3, May 1995, p. 65.

[5]Yudintsev, Y. N., and Chirkashenko, C. F., "Modes of Counterjet Interaction with a Supersonic Flow," *Gas Dynamics and Acoustics of Jet Flows*, Inst. of Theoretical and Applied Mechanics, Siberian Branch, Russian Academy of Sciences, Novosibirsk, Russia, 1979, pp. 75–107 (in Russian).

[6]Shang, J., "Plasma Actuator for Hypersonic Flow Control," AIAA Paper 2005-562, Jan. 2005.

[7]Klimov, A. I., Koblov, A. N., Mishin, G. I., Serov, Y. L., and Yavor, I. P., "Shock Wave Propagation in a Glow Discharge," *Soviet Technical Physics Letters*, Vol. 8, No. 4, 1982, pp. 192–194.

[8]Klimov, A. I., Koblov, A. N., Mishin, G. I., Serov, Y. L., and Yavor, I. P., "Shock Wave Propagation in a Decaying Plasma," *Soviet Technical Physics Letters*, Vol. 8, No. 5, 1982, pp. 240, 241.

[9]Ganguly, B. N., Bletzinger, P., and Garscadden, A., "Shock Wave Damping and Dispersion in Nonequilibrium Low Pressure Argon Plasmas," *Physics Letters A*, Vol. 230, June 1997, pp. 218–222.

[10]Leonov, S., Bityurin, V., and Kolesnichenko, Y., "Dynamic of a Single-Electrode HF Plasma Filament in Supersonic Airflow," AIAA Paper 2001-0493, Jan. 2001.

[11]Cain, T., and Boyd, D., "Electrodynamics and the Effect of an Electric Discharge on Cone/Cylinder Drag at Mach 5," AIAA Paper 99-0602, Jan. 1999.

[12]Ionikh, Y. Z., Chernysheva, N. V., Meshchanov, A. V., Yalin, A. P., and Miles, R. B., "Direct Evidence for Thermal Mechanism of Plasma Influence on Shock Wave Propagation," *Physics Letters A*, Vol. 259, No. 5, 1999, p. 387.

[13]Macharet, S. O., Martinelli, L., and Miles, R. B., "Shock-Wave Propagation and Structure in Non-Uniform Gases and Plasmas," AIAA Paper 99-0598, Jan. 1999.

[14]Macheret, S. O., Ionikh, Y. Z., Chernysheva, N. V., Yalin, A. P., Martinelli, L., and Miles, R. B., "Shock Wave Propagation and Dispersion in Glow Discharge Plasmas," *Physics of Fluids*, Vol. 13, No. 9, 2001, pp. 2693–2705.

[15]Riggins, D., Nelson, H. F., and Johnson, E., "Studies of Conical Shock-wave Modification by Nonequilibrium RF Discharge Plasma," *AIAA Journal*, Vol. 37, No. 4, 1999, pp. 460–467.

[16]Bailey, F., and Hilbun, W. M., "Baseline of Thermal Effects on Shock Propagation in Glow Discharge," *Proceedings of the 1st Weakly Ionized Gases Workshop*, U.S. Air Force Academy, 1997, pp. GG3–GG18.

[17]Kremeyer, K., Nazarenko, S., and Newell, A., "The Effect of Fore-Shock Heating in the Plasma Drag-Reduction Problem," AIAA Paper 2000-2700, June 2000.

[18]Kremeyer, K., Nazarenko, S., and Newell, A., "The Role of Vorticity in Shock Propagation Through Inhomogeneous Media," AIAA Paper 99-0871, Jan. 1999.

[19]Merriman, S., Christian, A., Meyer, R., Kowalczyk, B., Palm, P., and Adamovich, I., "Studies of Conical Shockwave Modification by Nonequilibrium RF Discharge Plasma," AIAA Paper 2001-0347, Jan. 2001.

[20]Ionikh, Y. K., Chernysheva, N. V., Yalin, A. P., Macheret, S. O., Martinelli, L., and Miles, R. B., "Shock Wave Propagation Through Glow Discharge Plasmas—Evidence of Thermal Mechanism of Shock Dispersion," AIAA Paper 2000-0714, Jan. 2000.

[21]Fomin, V., Tretyakov, P., and Taran, J.-P., "Flow Control Using Various Plasma and Aerodynamic Approaches (Short Review)," *Aerospace Science and Technology*, Vol. 8, No. 5, 2004, pp. 411–421.

[22]Bityurin, V., Klimov, A., Leonov, S., Popov, N., and Van Wie, D., "Shock Wave Structure and Velocity at Propagation Through Non-Homogeneous Plasma," AIAA Paper 2000-2571, June 2000.

[23]Bletzinger, P., Ganguly, B. N., and Garscadden, A., "Mutual Interactions Between Low Mach Number Shock Waves and Nonequilibrium Plasmas," AIAA Paper 2001-3050, June 2001.

[24]Siefert, N., and Ganguly, B., and Bletzinger, P., "Shockwave-Induced Enhancement of Optical Emission in Nitrogen Afterglow Plasma," AIAA Paper 2005-5372, June 2005.

[25]Kremeyer, K., Nazarenko, S., and Newell, A., "Shock Bowing and Vorticity Dynamics During Propagation into Different Transverse Density Profiles," *Physica D*, Vol. 163, No. 3, 2002, pp. 150–165.

[26]Diels, J.-C., "Tests of Laser-Induced Discharge of High DC Voltage Using High-Power Femtosecond UV Pulses," *Proceedings of Advanced High-Power Lasers and Applications*, edited by K. Mima, G. L. Kulcinski, and W. J. Hogan, Vol. 3886-23, Society of Photo-Optical Instrumentation Engineers (International Society for Optical Engineering), Bellingham, WA, 1999, pp. 158–166.

[27]Schwarz, J., Rambo, P. K., and Diels, J.-C., "Comparative Observations of Filaments at 248 nm and 800 nm," *Optics Communications* (submitted for publication).

[28]La Fontaine, B., Vidal, F., Jiang, Z., Chien, C. Y., Comtois, D., Desparois, A., Johnston, T. W., Kieffer, J.-C., Pepin, H., and Mercure, H. P., "Filamentation of Ultrashort Pulse Laser Beams Resulting from Their Propagation over Long Distances in Air," *Physics of Plasmas*, Vol. 6, 1999, pp. 1615–1621.

[29]Brodeur, A., Chien, C. Y., Ilkov, F. A., Chin, S. L., Kosareva, O. G., and Kandidov, V. P., "Moving Focus in the Propagation of Ultrashort Laser Pulses in Air," *Optics Letters*, Vol. 22, No. 5, 1997, pp. 304–306.

[30]Schwarz, J., and Diels, J.-C., "Long Distance Propagation of UV Filaments," *Journal of Modern Optics*, Vol. 49, No. 14/15, 2002, pp. 2583–2597.

[31]Kremeyer, K., USPTO, Patent Number 6,527,221 B1, May 2000.

[32]Adelgren, R. G., Elliot, G. S., Knight, D. D., Zheltovodov, A. A., and Beutner, T. J., "Energy Deposition in Supersonic Flows," AIAA Paper 2001-0885, Jan. 2001.

[33]Myrabo, L. N., and Raizer, Y., "Laser-Induced Air Spike for Advanced Transatmospheric Vehicles," AIAA Paper 94-2451, June 1994.

[34]Aleksandrov, V. N., Vidiakin, N. G., Lakutin, V. A., Skvortsov, J. G., and Timofeev, I. B., "On a Possible Mechanism of Interaction of a Shock Wave with the Decaying Plasma of a Laser Spark in Air," *Zhurnal Tekhnika Fizika*, Vol. 56, April 1986, p. 771.

[35]Rambo, P., Schwarz, J., and Diels, J.-C., "High-Voltage Electrical Discharges Induced by an Ultrashort-Pulse UV Laser System," *Journal of Optics A: Pure and Applied Optics*, Vol. 3, March 2001, pp. 146–158.

[36]Plooster, M. N., "Shock Waves from Line Sources, Numerical Solutions and Experimental Measurements," *Physics of Fluids*, Vol. 13, No. 11, 1970, pp. 2665–2675.

[37]Schreier, S., *Compressible Flow*, Wiley, New York, 1982, Chap. 5.

[38]Sachdev, P. L., "Propagation of a Blast Wave in Uniform or Non-Uniform Media: A Uniformly Valid Analytic Solution," *Journal of Fluid Mechanics*, Vol. 52, 1972, pp. 369–378.

[39]Lutzky, M., and Lehto, D. L., "Shock Propagation in Spherically Symmetric Exponential Atmospheres," *Physics of Fluids*, Vol. 11, No. 7, 1968, pp. 1466–1472.

[40]Plooster, M. N., "Erratum: Shock Waves from Line Sources. Numerical Solutions and Experimental Measurements," *Physics of Fluids*, Vol. 14, No. 10, 1971, p. 2248.

[41]Girgis, I. G., Shneider, M. N., Macheret, S. O., Brown, G. L., and Miles, R. B., "Creation of Steering Moments in Supersonic Flow by Off-Axis Plasma Heat Addition," AIAA Paper 2002-0129, Jan. 2002.

[42]Shneider, M. N., Macheret, S. O., Zaidi, S., Girgis, I. G., and Miles, R. B., "Steady and Unsteady Supersonic Flow Control with Energy Addition," AIAA Paper 2003-3862, June 2003.

[43]Georgievsky, P., and Levin, V., "Effective Flow-over-Body Control by Energy Input Upstream," AIAA Paper 2003-0038, Jan. 2003.

[44]Soloviev, V. R., Krivtsov, V. M., Konchakov, A. M., and Malmuth, N. D., "Drag Reduction by Plasma Filaments over Supersonic Forebodies," *AIAA Journal*, Vol. 41, No. 12, 2003, pp. 2403–2409.

[45]Harten, A., Engquist, B., Osher, S., and Chakravarthy, S., "Uniformly High Order Essentially Non-Oscillatory Schemes, III," *Journal of Computational Physics*, Vol. 71, No. 2, 1987, pp. 231–303.

[46]Liu, X.-D., Osher, S., and Chan, T., "Weighted Essentially Non-Oscillatory Schemes," *Journal of Computational Physics*, Vol. 115, No. 1, 1994, pp. 200–212.

[47]Friedrichs, O., "Weighted Essentially Non-Oscillatory Schemes for the Interpolation of Mean Values on Unstructured Grids," *Journal of Computational Physics*, Vol. 144, No. 1, 1998, pp. 194–212.

[48]Hu, C., and Shu, C.-W., "Weighted Essentially Non-Oscillatory Schemes on Triangular Meshes," *Journal of Computational Physics*, Vol. 150, No. 1, 1999, pp. 97–127.

[49]Shi, J., Hu, C., and Shu, C.-W., "A Technique of Treating Negative Weights in WENO Schemes," *Journal of Computational Physics*, Vol. 175, No. 1, 2002, pp. 108–127.

[50]Jiang, G., and Shu, C.-W., "Efficient Implementation of Weighted ENO Schemes," *Journal of Computational Physics*, Vol. 126, No. 1, 1996, pp. 202–228.

[51]Balsara, D., and Shu, C.-W., "Monotonicity Preserving Weighted Essentially Non-Oscillatory Schemes with Increasingly High Order of Accuracy," *Journal of Computational Physics*, Vol. 160, No. 2, 2000, pp. 405–452.

[52]Saltzman, E. J., "Base Pressure Coefficients Obtained from the X-15 Airplane for Mach Numbers up to 6," NASA TN D-2420, Aug. 1964.

[53]Sims, J., "Tables for Supersonic Flow Around Right Circular Cones at Zero Angle of Attack," NASA SP-3004, March 1964.

[54]Kremeyer, K., Sebastian, K., and Shu, C.-W., "Lines of Pulsed Energy: Shock Mitigation and Drag Reduction," AIAA Paper 2004-1131, Jan. 2004.

[55]Kremeyer, K., "Lines of Pulsed Energy for Supersonic/Hypersonic Drag Reduction: Generation and Implementation," AIAA Paper 2004-0984, Jan. 2004.